Compressional rate-dependent stability of ammonia hydrates crystallized from water-rich ammonia solutions

A. Mondal [1,2,*] K. Mohrbach,[1,3] K. Glazyrin [3] H.-P. Liermann [3] and C. Sanchez-Valle [1]
[1]*Institut für Mineralogie, Universität Münster, 48149 Münster, Germany*
[2]*Department of Physics, National Institute of Technology Agartala, 799046 Jirania, Tripura (W), India*
[3]*Deutsches Elektronen-Synchrotron DESY, Notkestr. 85, 22607 Hamburg, Germany*

(Received 7 December 2025; revised 15 July 2026; accepted 16 October 2026; published 6 November 2026)

Understanding the crystallization pathways of water-rich ammonia-water (NH_3-H_2O) solutions and the stability of ammonia hydrates is key to unraveling the behavior of complex hydrogen-bonding networks and to modeling planetary interiors. Yet there are still inconsistencies in the crystallization sequence reported upon pressure-induced crystallization of H_2O-rich NH_3-H_2O solutions at room temperature. Here, we investigate the effect of compression rates on the crystallization pathways of 25 wt% NH_3 aqueous solutions at room temperature using dynamically compressed diamond anvil cells (dDAC) coupled with time-resolved x-ray diffraction. We show that compression rates exceeding 0.5 GPa/sec promote direct crystallization of a body-centered cubic (bcc) phase (DMA') with possible AMH stoichiometry coexisting with ice VII, while rates below 0.2 GPa/sec stabilize monoclinic NH_3-rich AHH-II and ice VII phases. Intermediate rates between 0.2 and 0.5 GPa/sec produce a mixture of both hydrates alongside ice VII, hence demonstrating the role of compression rate on the crystallization sequence of ammonia solutions. The compression behavior and phase stability of the distinct phase assemblies (AHH-II/DMA' + ice VII) are investigated further to place constraints on the composition of the DMA' phase, the effect of ice VII on the compressibility of ammonia hydrates, and the plausible incorporation of NH_3 impurities within the lattice of high-pressure ice phases.

DOI: 10.1103/mw4m-12fz

I. INTRODUCTION

Understanding the phase behavior of the ammonia-water (NH_3-H_2O) system under extreme pressure-temperature (*P-T*) conditions is of critical importance in both materials physics [1] and planetary science [2]. As model hydrogen-bonded molecular systems [1], these binary mixtures exhibit crystallization behavior that is sensitive to stoichiometry and thermal history, making them ideal for studying metastable phase formation and kinetic effects under compression [3,4]. Furthermore, as important constituents of the mantles of icy moons [5] (e.g., Titan, Europa, etc.), the ice giant planets [6–8] (Uranus and Neptune), and ice-rich exoplanets [9–11], the stability of phases in the NH_3-H_2O system over a broad range of pressure-temperature conditions is critical in modeling their internal structure and thermal evolution. At room pressure, the crystallization of NH_3-H_2O solutions stabilizes three stoichiometrically distinct ammonia hydrate forms [12]: ammonia hemihydrate (AHH, $2NH_3$:$1H_2O$), ammonia monohydrate (AMH, $1NH_3$:$1H_2O$) and ammonia dihydrate (ADH, $1NH_3$:$2H_2O$). Despite extensive research efforts, significant discrepancies persist within the reported *P-T* phase diagrams [1,13–16], particularly in relation to the nucleation behavior [12,13,16] and phase stability [14–18] of ammonia hydrates. Upon compression at room temperature, NH_3-H_2O solutions undergo fractional crystallization that first stabilizes ice VII, followed by the crystallization of the residual NH_3-rich liquid into an ammonia hydrate phase whose nature remains a matter of debate [14,15]. For instance, the formation of the monoclinic AHH-II phase has been identified at pressures above 3.5 GPa [17,19,20], while studies by Boone *et al.* [15,16] have reported the formation of an AMH phase and ice VII upon crystallization of NH_3-H_2O solutions. Moreover, Wilson *et al.* [14] have reported the direct formation of an unidentified body-centered cubic (bcc) disordered molecular alloy (DMA) phase, unlike the AHH-II, in coexistence with ice VII at pressures as low as 7.6 GPa under rapid compression from 32 wt% NH_3-H_2O solutions at room temperature. These observations suggest that compression rates may significantly influence the phase relations, nucleation kinetics, and the crystallization pathways of novel stable or metastable phases [21,22]. Despite this potential importance, to the best of our knowledge, the role of compression rate in the crystallization of the NH_3-H_2O solutions has yet to be systematically explored.

To address this gap, we utilized diamond anvil cells with dynamic compression capabilities [23], in combination with time-resolved x-ray diffraction (XRD), to investigate the effect of compression rates ranging from 0.005 to 4 GPa/sec on the crystallization of 25 wt% NH_3-H_2O solutions at room temperature, 298 K. Our results reveal the formation of three

*Contact author: anshuman.phy@faculty.nita.ac.in

Published by the American Physical Society under the terms of the Creative Commons Attribution 4.0 International license. Further distribution of this work must maintain attribution to the author(s) and the published article's title, journal citation, and DOI.

TABLE I. Summary of experimental conditions, compression rates and characterized phase assemblies observed in the crystallization experiments of 25 wt% NH_3-H_2O solutions.

Run No.	Compression rate (GPa/sec)	Starting *P* (GPa)	Maximal *P* (GPa)	Phases
dDAC1	4	0.45	13	DMA' + ice VII
dDAC2	2	0.3	9.4	DMA'+ ice VII
dDAC3	0.5	1	6.6	AHH-II + DMA'+ ice VII
dDAC4	0.5	1.2	10.4	AHH-II + DMA'+ ice VII
dDAC5	0.2	0.6	19.2	AHH-II + DMA'+ ice VII
dDAC6	0.2	1.3	9.4	AHH-II + DMA'+ ice VII
dDAC7	0.2	0.4	11.6	AHH-II + DMA'+ ice VII
dDAC8	0.1	0.2	5.6	AHH-II+ ice VII
dDAC9	0.05	1.2	3.8	AHH-II+ ice VII
dDAC10	0.01	0.9	8.2	AHH-II+ ice VII
dDAC11	0.005	0.4	13.2	AHH-II+ ice VII

distinct phase assemblages depending on compression rate: (1) monoclinic AHH-II and ice VII assembly below 0.2 GPa/sec; (2) a bcc DMA phase (hereafter DMA') and ice VII assembly above 0.5 GPa/sec; and (3) AHH-II + DMA' + ice VII between 0.2 and 0.5 GPa/sec. The compression responses of the AHH-II + ice VII and DMA' + ice VII phase assemblages were examined further up to 93 and 146 GPa, respectively. These findings prompt further discussion into the structural identity of the DMA' phase, the influence of ice VII on the equation of state (EoS) of ammonia hydrates, and the potential incorporation of NH_3 impurities within the bcc ice VII lattice.

II. EXPERIMENTAL METHODS

A. Diamond anvil cell (DAC) preparations

Symmetric diamond anvil cells (DACs) equipped with type Ia diamonds with 150–200 μm culet diameter were utilized for the experiments. Rhenium (Re) gaskets, which were pre-indented to an approximate thickness of 30 μm and drilled with a central hole of half the size of diamond culet diameter, were employed as sample chambers. Compression runs were carried out using commercially available NH_3-H_2O solutions containing 25 wt% NH_3 (Sigma-Aldrich, product No. 1.05428). To prevent NH_3 evaporation from the solution during loading, the samples were refrigerated to approximately 278 K and the DAC pre-cooled to around 292 K as monitored using a thermocouple prior to loading. The loading procedure was carried out in a fume hood under ambient atmosphere without evidence of condensation during handling. A droplet of the solution was carefully placed into the sample chamber with a medical syringe, and the DAC was immediately closed and pressurized to minimize any possible change in composition. Fine-grained gold (Au) powders were introduced into the compression chamber to serve as pressure markers during the compression experiments [24].

Two different sets of experiments were performed in this study: (1) compression rate-dependent crystallization experiments on 25 wt% NH_3-H_2O solutions (0.005 to 4 GPa/sec compression rates) (Table I); and thereafter (2) *P-V* compression experiments on the identified crystalline assemblages from fast (>0.5 GPa/sec) and slow (<0.2 GPa/sec) compression rate experiments (Table II). For the crystallization experiments, the DACs were closed immediately after loading at pressures below 1.5 GPa so that the entire sample remained in the liquid state (Table I). Thereafter, a piezo-driven dynamic DAC (dDAC) [23] was used to accurately control the compression rate during the crystallization experiments. A total of eleven dDAC runs were performed by applying a trapezoidal voltage waveform with compression rates ranging from 0.005 to 4 GPa/sec (Table I). For the *P-V* compression experiments, 25 wt% NH_3-H_2O solutions were loaded into the compression chambers, and the DACs were mechanically pressurized in order to stabilize the AHH-II + ice VII and DMA' + ice VII assemblies identified in the compression rate-dependent crystallization studies, under both static and dynamic compression (Table II). In the dDAC 13 run, however, the starting solution partially crystallized as the initial mechanical compression only reached 2.5 GPa, i.e., only ice VII formed in coexistence with a NH_3-rich residual liquid [17], which only crystallized into DMA' at ∼6.4 GPa during the actual compression run (Table II). The investigated samples were pressurized using either a gas-driven membrane (mDAC) [25] or the dDAC [23] setup described above. For the mDAC runs, pressure was increased in steps of ∼0.5 GPa corresponding to the membrane gas pressure increase of ∼ 0.2 bar and a slew rate of 0.05 bar/sec (Table II). In the dDAC runs, a triangular voltage waveform was selected for ramp compressions with compression rates listed in Table II.

B. X-ray diffraction data collection and analysis

Angle-dispersive powder x-ray diffraction experiments were conducted at beamline P02.2 of PETRA III, DESY, Hamburg, Germany [26]. Powder XRD patterns were collected during compression runs using monochromatic synchrotron x rays focused to a beam spot size of $3 \times 8\,\mu m^2$ full width at half maximum (FWHM). The compression rate-dependent crystallization experiments were conducted employing an x-ray energy of 25.63 keV (Table I), while the incident x-ray energies for the four *P-V* compression experiments are listed in Table II. In the crystallization experiments, time-resolved XRD patterns were collected utilizing a PerkinElmer XRD1621 flat panel detector with an exposure time of 1 sec at different compression rates. In

TABLE II. Summary of P-V compression runs performed on AHH-II and DMA' phases coexisting with ice VII.

Run No.	Investigated assemblages	X-ray energy (keV)	Exposure time (sec)	Starting *P* (GPa)	Maximal *P* (GPa)	Slew (mDAC)/ Compression (dDAC) rate
mDAC1	AHH-II + ice VII	25.62	5	5.8	71.1	0.05 bar/sec
mDAC2	DMA'+ ice VII	42.65	5–10	8.8	146.4	0.05 bar/sec
dDAC12	AHH-II + ice VII	25.59	0.2	6	92.8	1 GPa/sec
dDAC13	DMA'+ ice VII	25.62	2	6.4	36.6	0.1 GPa/sec

addition, systematic x-ray diffraction maps were recorded with a step size of 5 μm and an exposure time of 0.2 sec at the highest-pressure plateau during the compression-rate-dependent (dDAC) crystallization experiment. For the P-V compression experiments, the XRD data were collected using the PerkinElmer XRD1621 flat panel detector, and two 2.3 MPix GaAs LAMBDA detectors [27,28] for mDAC and dDAC runs, respectively. The data acquisition times for all four compression runs are listed in Table II. Moreover, before compression, XRD maps were collected across the entire compression chamber with an exposure time of 0.5–1 sec to identify regions of high signal-to-noise ratio for further diffraction analysis.

The calibration of sample-to-detector distance, tilt, and rotation for XRD1621 or LAMBDA detectors was accomplished using x-ray standards (CeO_2 or Cr_2O_3 from NIST SRM 674b). The 2D diffractograms were integrated into one-dimensional (1D) diffraction patterns using the DIOPTAS software [29]. A quick visualization through an intensity plot (Fig. 1) stacking all diffractograms collected during the compression run was generated using the modified DIOPTAS software integrated in the P02.2 data pipeline [30]. The 2θ angle of individual reflections was determined based on a pseudo-Voigt fit using a Python least-squares fitting routine [31].

In the *P-V* compression experiments (Table II), the weak diffraction signal of the low-*Z* ammonia hydrate samples and the limited angular coverage offered by the 2.3 MPix LAMBDA detectors resulted in reduced 2θ-angle sampling in the dDAC runs compared to the mDAC experiments. Therefore only the (110) reflection of the bcc ammonia hydrate phases was observed throughout the entire pressure range in the dDAC experiments, compared to the two to three reflections in the static mDAC runs (Figs. S1 and S2 of Supplemental Material [32]). To facilitate direct comparison among all four datasets (Table II), the lattice parameters of the bcc AHH-D(I)MA and DMA' phases were determined using only the position of the (110) reflection. The uncertainty in volume of the bcc ammonia hydrate phases was estimated based on the standard deviation in the volumes determined from (110), (211), and/or (220) reflections in the diffraction data collected in the mDAC runs in the low-pressure ranges (Figs. S1 and S2 of Ref. [32] and Table II). We assumed the error in the volumes to be similar for the dDAC compression runs, as well as for the high-pressure mDAC XRD data. Spottiness in ice VII arising from stressed, coarse-grained (quasisingle crystal) crystallites resulted in the asymmetry and apparent splitting of the ice VII (110) reflection in various runs (e.g., Fig. 2 and Figs. S1, S2 of Ref. [32]). For volume determination, ice VII (110) reflections in all runs, including those exhibiting asymmetry or apparent splitting, were fitted with a single component. The resulting reflection position was used as an effective average d-spacing of the contributing diffracting crystallites, from which the lattice parameter and volume were calculated. Pressure determination relied on the position of the Au (111) reflection [33], which is known to be least sensitive to nonhydrostatic uniaxial stress [34]. Moreover, x-ray diffraction maps were visualized using X-ray Diffractive Imaging (XDI) software [35] and presented

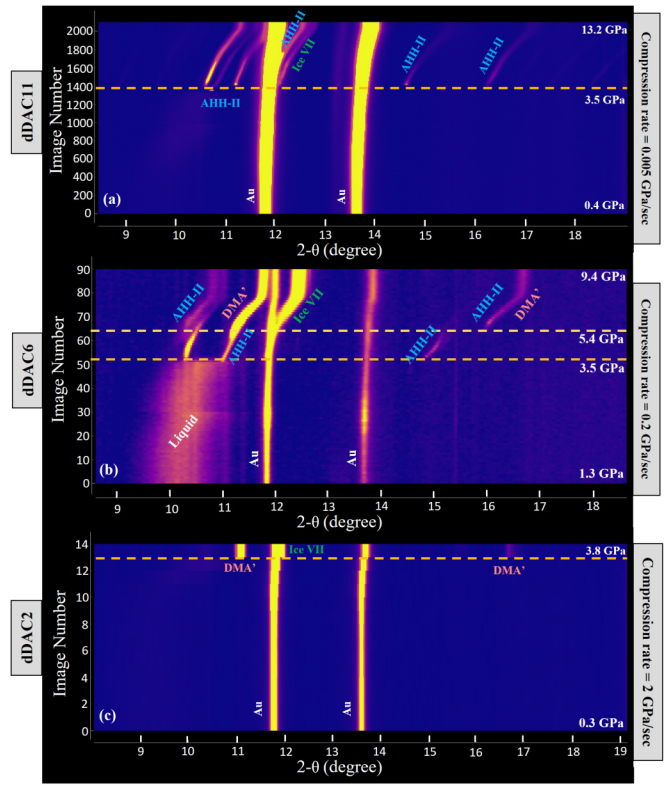


FIG. 1. Intensity plot displaying the stacking of all diffractograms collected in (a) dDAC11 (0.005 GPa/sec, Table I), (b) dDAC6 (0.2 GPa/sec, Table I), and (c) dDAC2 (2 GPa/sec, Table I) during ramp compressions. The 25 wt% NH_3-H_2O solutions crystallize into either (a) AHH-II phase, (b) the bcc DMA' phase, or (c) a mixture of both assemblages, depending on the compression rate. The pressure values indicate the initial and highest pressure in the ramp compressions and highlight the crystallization of different phases observed with increasing pressure from the liquid phase. In the dDAC6 run with intermediate compression rate, we were only able to identify the DMA' phase from ∼5.4 GPa onwards, due to the overlap of the DMA' (110) reflection with the (023) AHH-II reflection.

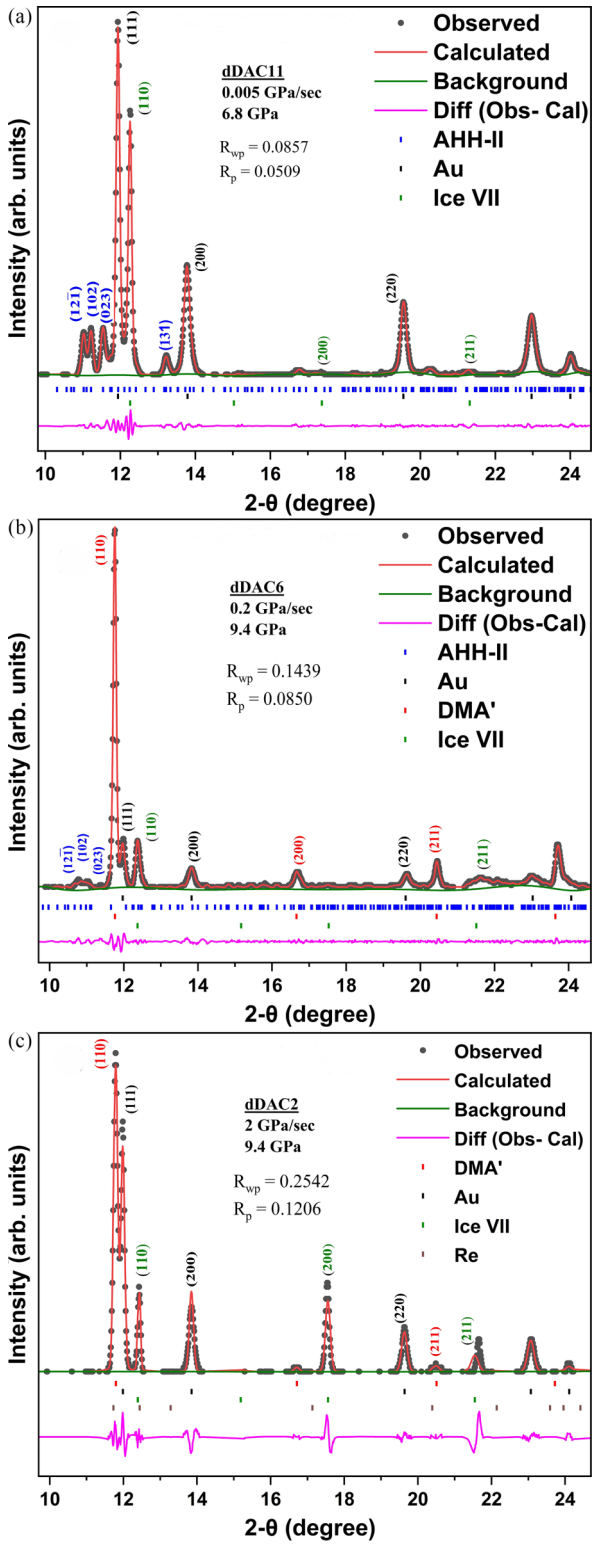


FIG. 2. Le Bail refinements of selected 1-dimensional (1D) x-ray diffraction patterns (x-ray energy = 25.63 keV) displaying the different phase assemblages crystallized from the 25 wt% NH_3-H_2O solution at the compression rates of (a) 0.005, (b) 0.2, and (c) 2 GPa/sec, respectively (Table I).

in Fig. S3 [32]. Analysis of the diffraction maps collected at the highest-pressure plateau during the compression-rate-dependent crystallization experiment indicates that the spatial pressure variations across the sample are relatively small, with pressure differences of approximately 0.1 GPa across different regions. The corresponding variations in unit-cell volume are also limited, amounting to approximately 0.04 Å^3 for DMA' and 0.045 Å^3 for ice VII. Furthermore, the bulk modulus (B_0) and its pressure-derivative (B_0') at ambient temperature were derived from fitting the dense P-V datasets to a third-order Birch-Murnaghan equation of state (BM EoS) using the EoSFIT7C program [36].

III. RESULTS AND DISCUSSION

A. Compressional rate-dependent stability of ammonia hydrates

The outcomes of the compression-rate-dependent crystallization experiments of the 25 wt% NH_3-H_2O solutions (dDAC runs) are summarized in Table I. The XRD maps recorded at the highest pressure plateau across the entire compression chamber (Fig. S3 [32]), along with the intensity plots stacking the integrated diffractograms collected during the compression ramps [Fig. 1(c)] reveal the formation of a bcc DMA-like phase [14], hereafter referred to as DMA', coexisting with ice VII, at compression rates exceeding 0.5 GPa/sec. This ammonia hydrate phase is identified by the characteristic bcc (110) reflection present at the 2θ angle of $\sim$11.79° [Fig. 2(c)]. Although neutron diffraction data are not available to confirm the disordered nature of the phase, we infer this phase to be DMA-like, which appears to be the thermodynamically stable phase of ammonia hydrates at high pressure [14]. Additionally, the FWHM of the DMA' reflections is found to be higher in comparison to the reflections arising from known ordered structures (AHH-II or Au) in the XRD spectra, further supporting the hypothesis of intrinsic disorder. In contrast, compression rates below 0.2 GPa/sec stabilize the monoclinic AHH-II structure [14,17], in coexistence with ice VII, as indicated by the characteristic $(12\bar{1})$, (102), and (023) reflections in the 11 to 12 deg 2θ angle region [Fig. 2(a)]. Interestingly, compression rates between 0.2 and 0.5 GPa/sec yield a mixture of both ammonia hydrate phases (DMA' + AHH-II), together with ice VII, which are heterogeneously distributed within the compression chamber (Fig. S3(b) [32]). Only a limited number of small regions across the compression chamber exhibited sufficient signal-to-noise ratio where the three-phase assemblage (AHH-II + DMA' + ice VII) could be reliably identified, which precluded further P-V compression studies to higher pressures. Moreover, the fractions of the individual ammonia hydrate phases could not be extracted from the recorded diffractograms as the presence of large crystallites prevented the formation of homogeneous powder rings. Representative XRD patterns recorded at compression rates of 0.005, 0.2, and 2 GPa/sec, together with their corresponding Le Bail refinements, are displayed in Fig. 2.

These observations confirm that the compression rate plays a pivotal role in the crystallization pathway of ammonia-water solutions containing 25 wt% NH_3, leading to the formation of distinct phase assemblages. The present results thus resolve discrepancies in the phase relations previously reported for the crystallization of H_2O-rich NH_3-H_2O solutions [14]. An updated pressure-temperature phase diagram for the 25 wt% NH_3-H_2O system, modified after Mousis *et al.* [13]

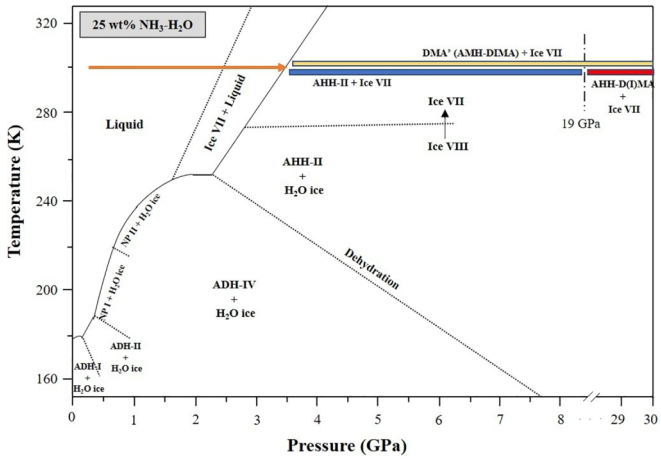


FIG. 3. Pressure-temperature phase diagram of 25 wt% NH_3-H_2O system modified after Mousis *et al.* [13] and Wilson *et al.* [14] based on the results of the present compression-rate-dependent crystallization studies. The solution crystallizes to either AHH-II phase + ice VII (color-coded in blue, compression rate <0.2 GPa/sec) or the DMA' phase (color-coded in yellow, compression rate >0.5 GPa/sec) or in a mixture of the two assemblages in the intermediate compression rate ranges. Above approximately 19 GPa, the AHH-II + ice VII assemblage transforms into AHH-D(I)MA + ice VII (color-coded in red). The new phases (NP)-I and II are taken from the previous study by Mousis *et al.* [13] on 25 wt% NH_3-H_2O system, the structures of which are yet to be constrained.

and Wilson *et al.* [14], is presented in Fig. 3. This revised phase diagram provides a more comprehensive understanding of the compression-dependent stability of ammonia hydrates crystallized from H_2O-rich NH_3-H_2O solutions and serves as a foundation for further investigation into their structural and thermodynamic properties. While the stoichiometry of the DMA' phase cannot be directly inferred in the absence of single-crystal XRD data, we present an estimate of the composition by investigating its compressional behavior in comparison with the *P-V* curves of other known DMA/DIMA phases in the NH_3-H_2O system, as presented below.

B. Pressure evolution of the AHH-II and DMA' phases

High-pressure *P-V* compression experiments were performed on the two-phase assemblages, i.e., AHH-II + ice VII and DMA' + ice VII identified from the slow (<0.2 GPa/sec) and fast (>0.5 GPa/sec) compression of 25 wt% NH_3-H_2O solutions. The reduced signal-to-noise ratio displayed by the spectra showing the coexistence of AHH-II + DMA' + ice VII at intermediate (0.2–0.5 GPa/sec, Table I) compression rates precluded further P-V compression studies in the three-phase assembly. Selected diffractograms recorded upon compression of the AHH-II + ice VII and DMA' + ice VII assemblies in both membrane-driven mDAC (mDAC1, mDAC2) and piezo-driven dDAC runs (dDAC12, dDAC13) are presented in Figs. S1 and S2 of Ref. [32], respectively. In mDAC1 and dDAC12 runs (Fig. S1 [32]), the crystallized ammonia hydrate phase is identified as monoclinic AHH-II [17]. Upon further compression above 19 GPa, these three reflections merge into a single broad reflection, indicating the transformation into the bcc AHH-D(I)MA structure (Fig. S1 [32]). The transition pressure aligns well with previous reports [14,19,37,38] despite the presence of ice VII in the sample chamber. The phase appears stable up to 93 GPa without detectable changes in the pattern that would indicate the spontaneous partial ionization of the phase reported above 26 GPa on the basis of Raman spectroscopic measurements [38,39]. Because XRD analysis is not sufficiently sensitive to changes in the hydrogen bonding network, the partially ionic characteristics of the AHH-D(I)MA phase could not be resolved. We note that to date, evidence of partial ionization has only been detected in the ammonia monohydrate (AMH)-DIMA phase using XRD measurements. Moreover, the transformation to a purely ionic $P\bar{3}m1$ structure above 69 GPa [39] was not observed either.

The XRD spectra collected in run mDAC2 confirmed the crystallization of the bcc-structured ammonia hydrate DMA' and ice VII phases upon initial rapid mechanical compression of the 25 wt% NH_3-H_2O solution (Fig. S2(a) [32]). For run dDAC13, initial mechanical compression up to 2.5 GPa resulted in partial crystallization of the NH_3-H_2O solution (Fig. S2(b) [32]). Only upon further compression above ∼ 4 GPa, the DMA' phase and ice VII assembly became stable. Analysis of both mDAC2 and dDAC13 runs demonstrates that the bcc structure of the DMA' phase is stable up to 146 GPa, the highest pressure investigated in these experiments (Table II). Similar to our previous discussion, Raman spectroscopic measurements will be necessary to confirm whether partial ionization of this phase occurred at higher pressures. As reported in other studies on DMA/DIMA phases of the NH_3-H_2O system [40,41], their partially ionic counterparts, if present, may exist in minor fractions within the compression chamber and could remain undetected in XRD patterns due to their very weak contribution to the overall scattering signal.

C. Stoichiometry of DMA' based on *P-V* compression curves

The pressure dependence of the DMA' phase volume (per molecule) obtained from both mDAC and dDAC compression runs (Table II and Table S1 [32]) is depicted in Fig. 4 together with those for AHH-D(I)MA. Both the diffraction patterns and the P-V compression data of the AHH-D(I)MA phase are in good agreement with previous data reported in the literature [14,37,38]. Moreover, the volume (per molecule) of AHH-D(I)MA is found to be higher than that of the bcc DMA' phase, with differences of approximately 7% at 30 GPa (Fig. 4). In order to identify the probable stoichiometric composition of the DMA' phase, we compared its volume with all known stable ammonia hydrate DMA and/or DIMA phases [14,31,37,41–43] as well as with the end members H_2O [44] and NH_3 [45] (Fig. 4). Because the compression curve of the DMA' phase lies closer to the pure ice VII curve than that of the AHH-D(I)MA phase, it indicates a higher H_2O content in the DMA' phase. The composition of the DMA' phase can be further assessed tentatively by comparing with the diffractograms and P-V compression curve reported for the AMH-DIMA [42], which has a known 1:1 NH_3 to H_2O molar ratio. The good agreement between these two compression curves within their respective uncertainties, especially at pressures below 30 GPa and above 60 GPa (Fig. 4),

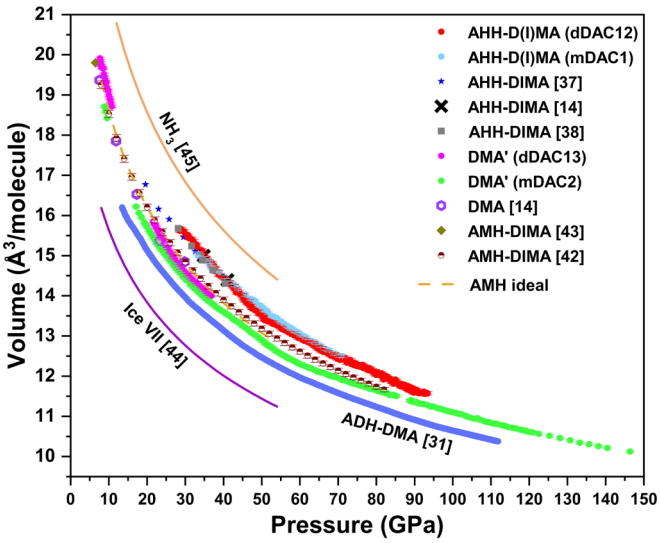


FIG. 4. Comparison of pressure-volume data between AHH-D(I)MA and DMA' phases (circles), derived from the evolution of the (110) reflection in all four compression experiments listed in Table II. The available compression data for DMA/DIMA phases within the NH_3-H_2O system, including pure NH_3 [45] and ice VII [44], are reported for comparison. The lack of volume data for DMA' in the ∼10–20 GPa pressure range results from the overlap between the main DMA' (110) reflection and the (111) reflection of the Au pressure marker, which prevents reliable refinement of the DMA' unit-cell parameters.

is consistent with an AMH-like ($1NH_3$:$1H_2O$) composition. The differences in the intermediate pressure range of the *P-V* curves may be due to the presence of ice VII in the compression chamber, which may develop locally distinct stress conditions [46,47] that affect the elastic response of the DMA' phase. Alternatively, this difference may also be interpreted as a possible exchange of NH_3 between the DMA' crystal lattice and the coexisting ice VII, which will be discussed in the following section.

While the stress conditions of the sample could not be constrained from the current data to identify the possible origin of the deviation in the volume compression curves, we note that DMA' phase volumes are in excellent agreement with those reported by Wilson *et al.* [14] for the bcc DMA phase observed in coexistence with ice VII crystallized upon rapid compression of 32 wt% NH_3-H_2O solutions (Fig. 4). Similarly, as described before, the overall compression behavior of DMA' is in good agreement with that reported for the AMH-DIMA phase by Zhang *et al.* [42] (Fig. 4). These observations suggest that DMA', the DMA phase of Wilson *et al.* [14], and the AMH-DIMA phase of Zhang *et al.* [42] are likely the same phase, or at least very closely related structural variants. However, the available diffraction and compression data do not uniquely constrain the exact stoichiometry or crystallographic identity of the DMA' phase in the absence of single-crystal structural refinements. Furthermore, signatures of the partially ionic counterpart of the DMA'/AMH-DIMA phase could not be identified from our XRD data as opposed to previous reports [40,48].

Finally, we compared the *P-V* data for the DMA' phase with that of an ideal AMH-DIMA phase (hereafter referred to as "AMH ideal") calculated by linear mixing of the ice VII [44] and NH_3 [45] volumes (Fig. 4). It is worth noting that the compression behavior of the DMA'/AMH-DIMA phase closely follows the ideal curve, particularly at low pressures (<20 GPa), which contrasts with the results from a previous compression study on the ADH-DMA phase [31]. This discrepancy in compression behavior at low pressures between the two different compositions could potentially originate from the complexity of the H-bonding network [43] and might be linked to the higher H_2O concentration in the ADH-DMA phase, which causes it to deviate from its ideal behavior.

D. Equation of state of DMA/DIMA phases in the NH_3-H_2O system

We have fitted the *P-V* datasets for the AHH-D(I)MA and DMA' phases (Table S1 [32]), including their associated errors, to a third-order BM EoS for comparison with previous studies (Figs. S4(a) and S4(b) of Ref. [32]). We adopted initial values of the ambient pressure volume (V_0) assuming an ideal mixing between NH_3 [45] and H_2O [44] with a 2:1 molar ratio for AHH-D(I)MA and a 1:1 ratio for DMA', and later refined the V_0 values until convergence. The best-fit EoS parameters are compared with all three stable ammonia hydrate DMA/DIMA forms in Table III. The fit parameters obtained for the AHH-D(I)MA phase are in good agreement with previously reported values [38]. The EoS parameters for the DMA' phase display a higher bulk modulus value compared to both the AHH-D(I)MA and ADH-DMA phases. We note that Zhang *et al.* [42] fixed the pressure derivative of the bulk modulus (B'_0) of the AMH-DIMA phase to the value reported for AMH-I, whereas in the present study B'_0 was refined independently. This is because AMH-I and AMH-DIMA (DMA') are crystallographically distinct phases and therefore are not necessarily expected to exhibit identical compression behavior. However, the refined B'_0 value obtained here remains very close to that reported by Zhang *et al.* [42], indicating that the differences in B_0 do not arise from the treatment of B_0'. Instead, they most likely reflect the substantially larger P-V range covered in the present study, extending to significantly higher pressures than the ∼80 GPa limit of the previous work [42]. Consequently, the present dataset provides tighter constraints on the overall compression behavior of the DMA' phase. The *P-V* data of DMA' are therefore consistent with those reported previously for the AMH-DIMA phase [42] and support the interpretation that DMA' is closely related to this phase and likely possesses a composition near the AMH stoichiometry. However, while the present diffraction and compression data are consistent with an AMH-like composition, they do not uniquely constrain the exact NH_3 ratio of the DMA' phase.

To further evaluate the quality of the EoS-fit, the residuals between the measured volumes and those calculated from the corresponding third-order BM fits were examined (Figs. S4(c) and S4(d) of Ref. [32]). The residuals are not entirely randomly distributed and exhibit systematic, run-dependent variations for both phases. Nevertheless, none of these residual patterns provide evidence for a structural transition or the onset of a distinct compression regime. Separate BM EoS fits performed below and above approximately 50–60 GPa did not

TABLE III. Birch-Murnaghan equation of state parameters for ammonia hydrate DMA/DIMA phases in the NH_3-H_2O system.

EoS parameters	AHH-D(I)MA (this work)	AHH-DIMA [38]	DMA' (this work)	AMH-DIMA [42]	ADH-DMA [31]
V_0 (Å^3/molecule)	29.25 ± 0.07	29.1 ± 0.2	25.93 ± 0.02	25.93 ± 0.03	23.96 ± 0.03
B_0 (GPa)	9.89 ± 0.01	9.6 ± 0.3	10.97 ± 0.04	12.17 ± 0.05	9.95 ± 0.14
B_0'	4.85 ± 0.02	4.6 ± 0.3	5.47 ± 0.01	5.3 (fixed)	6.59 ± 0.03

significantly improve the fitting quality relative to a single fit over the complete pressure range. The observed residual trends may therefore reflect run-dependent systematic effects, including differences in compression rate, increasing nonhydrostatic stresses, pressure gradients, or chemical interactions between coexisting phases. For DMA', the pressure interval showing the strongest residual curvature broadly overlaps the range over which the coexisting ice VII phase deviates from previously reported equations of state (Fig. 5). This correspondence may indicate a common stress environment or interactions between the coexisting phases, potentially including compositional redistribution or NH_3 incorporation into ice VII. However, the available data do not allow these possibilities to be distinguished unambiguously.

E. Plausible incorporation of NH_3 impurities in H_2O ice and effects on its compressibility

The present work also permits us to examine the high-pressure behavior of H_2O ice in the presence of ammonia hydrates, and particularly, whether NH_3 molecules may be incorporated into the crystal lattice of ice VII. The *P-V* data obtained for H_2O ice in all four compression runs (Table II and Table S2 [32]) are compared in Fig. 5. The results from mDAC1 and dDAC12 runs in the presence of the AHH-II/AHH-D(I)MA phase (Table II) are in good agreement with the pure H_2O ice data previously reported in the literature [44,49]. This agreement is expected because the more compressible AHH [38], with its lower bulk modulus, would not significantly influence the compression behavior of H_2O ice [44] crystals. However, the H_2O ice volume data collected in mDAC2 and dDAC13 runs, where it coexists with the DMA' phase (Table II), deviate from the other datasets between 30 and 60 GPa, with maximal differences of ≈–3% at 38 GPa. This observation thus suggests a different compression behavior of H_2O ice depending on whether it coexists with the AHH-D(I)MA or the DMA' phase in the sample chamber. Since DMA' is less compressible than AHH and has a compressibility somewhat closer to that of ice VII, its presence likely alters the overall compression behavior of H_2O ice observed in these runs. Interestingly, the deviation in the ice VII volume is observed in the same pressure range as the deviation of the coexisting DMA' phase volumes from the AMH-DIMA compression curve [42] (see discussion above).

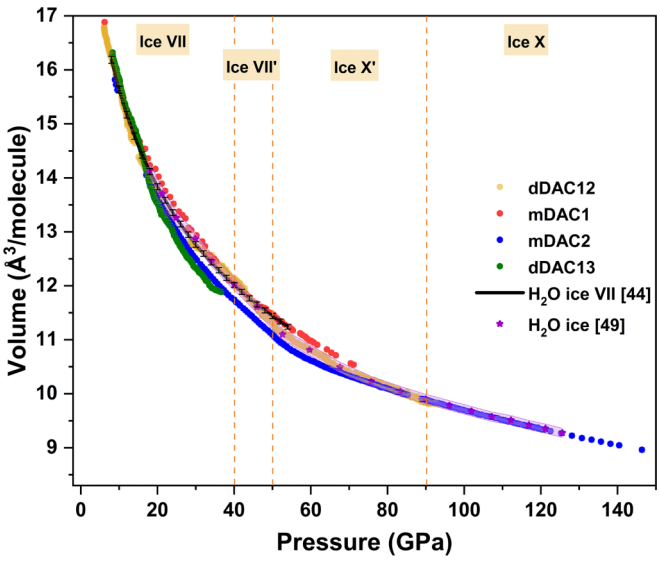


FIG. 5. Pressure-volume data of H_2O ice coexisting with the ammonia hydrates (AHH-II/AHH-D(I)MA and DMA') in four different compression runs (Table II) and comparison with literature data [44,49]. The vertical dashed lines indicate the stability field of the different H_2O ice polymorphs [49]. The negative volume deviations observed for ice VII coexisting with DMA' above ∼20–30 GPa may reflect the incorporation of NH_3 impurities within the ice VII lattice, although alternative explanations such as deviatoric stress effects and phase-interaction effects cannot presently be excluded. Above 60 GPa, H_2O ice volume data from all four compression runs tend to match again, suggesting a more ideal behavior at higher pressures.

While we cannot rule out that the observations are related to deviatoric stresses developed in the compression chamber, the reproducibility in both the mDAC2 and dDAC13 experiments suggests that the deviations could alternatively be explained by the incorporation of NH_3 impurities into the ice VII crystal lattice, consistent with the deviation observed in the compression curve of the DMA' phase. Although there are no previous reports on NH_3 incorporation into ice VII at high pressures, earlier XRD experiments have suggested the possibility of incorporating up to 1.6 mol% NaCl, 5 mol% CH_3OH, and 1.8 mol% $CaCl_2$ into the interstitial sites of the bcc ice VII crystal lattice, which resulted in volume changes that are comparable to this study, i.e., −4.5% for NaCl [50,51], +1.2% for CH_3OH [52], and −3% for $CaCl_2$ [47]. This variation in volume change arises from the distinct chemical pressures exerted by the incorporated species [47]. While larger cations like Ca^{2+} and Na^+ induce lattice compression, i.e., volume reduction, CH_3OH incorporation leads to expansion of the ice VII lattice. Similarly, if NH_3 were incorporated, its larger radius (effective crystal radius of 1.82 Å [53]) would decrease the volume by exerting stronger chemical pressure on the lattice, leading to the compression effect that is observed here. The geometry of the ice VII structure in fact does not exclude such incorporation. Klotz *et al.* [54] described relatively large octahedral interstitial cavities within ice VII, with characteristic edge lengths of approximately 3.39 Å along the unit-cell edge and 2.86 Å along the body diagonal. Therefore, particularly when local lattice relaxation and distortion are considered, the incorporation of NH_3 species into interstitial

regions of the ice VII framework cannot be ruled out on geometric grounds alone.

We also consider the formation of a substitutionally disordered molecular alloy between H_2O and NH_3 to be less consistent with the present observations. The volume reduction measured in our experiments is relatively small, approximately 3%, and is comparable to the changes previously attributed to limited interstitial incorporation of impurity species in ice VII [47,50–52]. A more extensive molecular-alloy formation would likely be expected to produce more substantial modifications to the lattice volume and compression behavior. Nevertheless, the present powder-diffraction data do not permit the precise location, concentration, or spatial distribution of any incorporated NH_3 species to be determined. Therefore detailed single-crystal structural refinement would be required to distinguish conclusively between interstitial incorporation, substitutional disorder, and stress-related effects.

Above 60 GPa, the H_2O ice volume is in better agreement within all four different compression runs (Fig. 5), and consistent with data reported for H_2O ice X' and ice X [49]. This suggests either a reduction of the effect responsible for the observed volume deviation at higher pressures or, if impurity incorporation occurs, a change in the behavior of NH_3-derived species within the H_2O ice lattice.

IV. CONCLUSION

Our study provides a comprehensive understanding of the influence of compression rates on the crystallization pathways of H_2O-rich NH_3-H_2O solutions (25 wt% NH_3), resolving discrepancies in the previously reported phase relations and crystallization processes. With the Le Bail refinements, we demonstrate that compression rates significantly affect the crystallization of distinct ammonia hydrate phases, with rates above 0.5 GPa/sec favoring the direct formation of the bcc DMA' phase, while rates below 0.2 GPa/sec stabilize the monoclinic AHH-II phase, both coexisting with ice VII. Intermediate rates between 0.2 and 0.5 GPa/sec produce a mixture of both hydrates alongside ice VII. We show that AHH-II transforms into the bcc AHH-D(I)MA phase above 19 GPa, in agreement with previous studies [37], and thereafter this phase remains stable up to 93 GPa in the presence of ice VII. In contrast, the DMA' phase was identified to remain stable up to 146 GPa without any evidence of phase transformations. Our detailed *P-V* comparison of these two assemblages suggested that the DMA' phase displays higher H_2O content compared to AHH. Based on the pressure evolution of the DMA' phase volume, we infer that this phase is closely related to the AMH-DIMA phase and is consistent with a composition near the AMH stoichiometry, although direct confirmation by single-crystal diffraction or chemical analysis is not currently available. Additionally, our results suggest possible incorporation of NH_3 into the ice VII lattice at high pressures, contributing to a deeper understanding of the stability and structural transitions of ammonia hydrates under extreme conditions. The implications of these findings extend beyond the fundamental behavior of hydrogen-bonded systems under compression, providing valuable insights into the role of compression rates in crystallization and metastable phase stability in NH_3-H_2O mixtures. These insights are crucial for modeling the phase behavior of H_2O-rich planetary bodies and provide evidence of the complex chemistry and physics of icy exoplanets and moons.

ACKNOWLEDGMENTS

This research was supported by the German Science Foundation (DFG) through Research Unit FOR 2440/2 (Grant No. SA2585/5–1). We acknowledge DESY (Hamburg, Germany), a member of the Helmholtz Association, for providing access to the experimental facility PETRA III and beamline P02.2. We also acknowledge the scientific exchange and support of the Centre for Molecular Water Science (CMWS). We also want to thank P02.2 beamline engineer M. Wendt for his useful technical support, and two anonymous reviewers for their valuable comments that helped to improve the manuscript.

DATA AVAILABILITY

The collected raw XRD data are available upon request to the corresponding author. The Python routine employed to extract the peak positions of individual reflections from the XRD patterns is available online at [55].

[1] J. S. Loveday and R. J. Nelmes, The ammonia hydrates—model mixed-hydrogen-bonded systems, High Pressure Res. **24**, 45 (2004).

[2] A. D. Fortes and M. Choukroun, Phase behaviour of ices and hydrates, Space Sci. Rev. **153**, 185 (2010).

[3] C. M. Pépin, R. André, F. Occelli, F. Dembele, A. Mozzanica, V. Hinger, M. Levantino, and P. Loubeyre, Metastable water at several compression rates and its freezing kinetics into ice VII, Nat. Commun. **15**, 8239 (2024).

[4] Y.-H. Lee, J. K. Kim, Y.-J. Kim, M. Kim, Y. C. Cho, R. J. Husband, C. Strohm, E. Ehrenreich-Petersen, K. Glazyrin, T. Laurus, H. Graafsma, R. P. C. Bauer, F. Lehmkühler, K. Appel, Z. Konôpková, M. Tang, A. P. Dwivedi, J. Sztuck-Dambietz, L. Randolph, K. Buakor, O. Humphries, C. Baehtz, T. Eklund, L. K. Mohrbach, A. Mondal, H. Marquardt, E. F. O'Bannon, K. Amann-Winkel, C.-S. Yoo, U. Zastrau, H.-P. Liermann, H. Nada, and G. W. Lee, Multiple freezing–melting pathways of high-density ice through ice XXI phase at room temperature, Nat. Mater. **25**, 302 (2026).

[5] H. Hussmann, C. Sotin, and J. I. Lunine, Interiors and evolution of icy satellites, *Treatise on Geophysics*, 2nd ed., edited by G. Schubert (Elsevier, Amsterdam, 2015), Vol. 10, pp. 605–635.

[6] W. B. Hubbard and J. J. MacFarlane, Structure and evolution of uranus and neptune, J. Geophys. Res. **85**, 225 (1980).

[7] J. J. Fortney and N. Nettelmann, The interior structure, composition, and evolution of giant planets, Space Sci. Rev. **152**, 423 (2010).

[8] R. Helled, N. Nettelmann, and T. Guillot, Uranus and neptune: Origin, evolution and internal structure, Space Sci. Rev. **216**, 38 (2020).

[9] W. J. Borucki, D. Koch, G. Basri, N. Batalha, T. Brown, D. Caldwell, J. Caldwell, J. Christensen-Dalsgaard, W. D.

Cochran, E. DeVore, E. W. Dunham, A. K. Dupree, T. N. Gautier, J. C. Geary, R. Gilliland, A. Gould, S. B. Howell, J. M. Jenkins, Y. Kondo, D. W. Latham, G. W. Marcy, *et al.*, Kepler planet-detection mission: Introduction and first results, Science **327**, 977 (2010).

[10] N. M. Batalha, J. F. Rowe, S. T. Bryson, T. Barclay, C. J. Burke, D. A. Caldwell, J. L. Christiansen, F. Mullally, S. E. Thompson, T. M. Brown, A. K. Dupree, D. C. Fabrycky, E. B. Ford, J. J. Fortney, R. L. Gilliland, H. Isaacson, D. W. Latham, G. W. Marcy, S. N. Quinn, D. Ragozzine, *et al.*, Planetary candidates observed by *KEPLER* . III. Analysis of the first 16 months of data, ApJS **204**, 24 (2013).

[11] L. Noack, I. Snellen, and H. Rauer, Water in extrasolar planets and implications for habitability, Space Sci. Rev. **212**, 877 (2017).

[12] J. S. Kargel, Ammonia-water volcanism on icy satellites: Phase relations at 1 atmosphere, Icarus **100**, 556 (1992).

[13] O. Mousis, J. Pargamin, O. Grasset, and C. Sotin, Experiments in the NH_3-H_2O system in the [0, 1 GPa] pressure range - implications for the deep liquid layer of large icy satellites, Geophys. Res. Lett. **29**, 2192 (2002).

[14] C. W. Wilson, C. L. Bull, G. W. Stinton, D. M. Amos, M.-E. Donnelly, and J. S. Loveday, On the stability of the disordered molecular alloy phase of ammonia hemihydrate, J. Chem. Phys. **142**, 094707 (2015).

[15] S. Boone and M. F. Nicol, Ammonia-water mixtures at high pressures - Melting curves of ammonia dihydrate and ammonia monohydrate and a revised high-pressure phase diagram for the water-rich region, Lunar. Planet. Sci. Conf. **21**, 603 (1991).

[16] M. L. Johnson and M. Nicol, The ammonia-water phase diagram and its implications for icy satellites, J. Geophys. Res. **92**, 6339 (1987).

[17] C. W. Wilson, C. L. Bull, G. Stinton, and J. S. Loveday, Pressure-induced dehydration and the structure of ammonia hemihydrate-II, J. Chem. Phys. **136**, 094506 (2012).

[18] A. D. Fortes, I. G. Wood, M. Alfredsson, L. Vočadlo, K. S. Knight, W. G. Marshall, M. G. Tucker, and F. Fernandez-Alonso, The high-pressure phase diagram of ammonia dihydrate, High Press. Res. **27**, 201 (2007).

[19] X. Li, W. Shi, X. Liu, and Z. Mao, High-pressure phase stability and elasticity of ammonia hydrate, Am. Mineral. **104**, 1307 (2019).

[20] A. Mondal, K. Mohrbach, T. Fedotenko, M. Bethkenhagen, H.-P. Liermann, and C. Sanchez-Valle, Reactions in the NH_3-H_2O system stabilize ultra-water-rich ammonia hydrates in the mantle layers of icy exoplanets, arXiv:2508.11924.

[21] G. W. Lee, W. J. Evans, and C.-S. Yoo, Crystallization of water in a dynamic diamond-anvil cell: Evidence for ice VII-like local order in supercompressed water, Phys. Rev. B **74**, 134112 (2006).

[22] A. Howard, M. Kim, J. Smith, and C.-S. Yoo, Dynamic compression effects of H_2O in a dynamic diamond anvil cell: Origin of metastable ice VII and its crystal growth kinetics, Phys. Rev. B **111**, 104105 (2025).

[23] Z. s. Jenei, H. P. Liermann, R. Husband, A. S. J. Méndez, D. Pennicard, H. Marquardt, E. F. O'Bannon, A. Pakhomova, Z. Konopkova, K. Glazyrin, M. Wendt, S. Wenz, E. E. McBride, W. Morgenroth, B. Winkler, A. Rothkirch, M. Hanfland, and W. J. Evans, New dynamic diamond anvil cells for tera-pascal per second fast compression x-ray diffraction experiments, Rev. Sci. Instrum. **90**, 065114 (2019).

[24] D. L. Heinz and R. Jeanloz, The equation of state of the gold calibration standard, J. Appl. Phys. **55**, 885 (1984).

[25] R. Letoullec, J. P. Pinceaux, and P. Loubeyre, The membrane diamond anvil cell: A new device for generating continuous pressure and temperature variations, High Pressure Res. **1**, 77 (1988).

[26] H.-P. Liermann, Z. Konôpková, W. Morgenroth, K. Glazyrin, J. Bednarčik, E. E. McBride, S. Petitgirard, J. T. Delitz, M. Wendt, Y. Bican, A. Ehnes, I. Schwark, A. Rothkirch, M. Tischer, J. Heuer, H. Schulte-Schrepping, T. Kracht, and H. Franz, The extreme conditions beamline P02.2 and the extreme conditions science infrastructure at PETRA III, J. Synchrotron. Rad. **22**, 908 (2015).

[27] D. Pennicard, S. Lange, S. Smoljanin, H. Hirsemann, H. Graafsma, M. Epple, M. Zuvic, M.-O. Lampert, T. Fritzsch, and M. Rothermund, The LAMBDA photon-counting pixel detector, J. Phys.: Conf. Ser. **425**, 062010 (2013).

[28] D. Pennicard, S. Smoljanin, F. Pithan, M. Sarajlic, A. Rothkirch, Y. Yu, H. P. Liermann, W. Morgenroth, B. Winkler, Z. Jenei, H. Stawitz, J. Becker, and H. Graafsma, LAMBDA 2M GaAs—A multi-megapixel hard X-ray detector for synchrotrons, J. Inst. **13**, C01026 (2018).

[29] C. Prescher and V. B. Prakapenka, *DIOPTAS* : A program for reduction of two-dimensional X-ray diffraction data and data exploration, High Press. Res. **35**, 223 (2015).

[30] M. Karnevskiy, K. Glazyrin, Y. Yu, A. Mondal, C. Sanchez-Valle, H. Marquardt, R. J. Husband, E. O'Bannon, C. Prescher, A. Barty, and H.-P. Liermann, Automated pipeline processing X-ray diffraction data from dynamic compression experiments on the Extreme Conditions Beamline of PETRA III, J. Appl. Cryst. **57**, 1217 (2024).

[31] A. Mondal, R. J. Husband, H.-P. Liermann, and C. Sanchez-Valle, Equation of state of ammonia dihydrate up to 112 GPa by static and dynamic compression experiments in diamond anvil cells, Phys. Rev. B **107**, 224108 (2023).

[32] See Supplemental Material at http://link.aps.org/supplemental/10.1103/mw4m-12fz for additional pressure-dependent x-ray diffraction patterns, diffraction maps from selected dynamic compression experiments, Birch-Murnaghan equation of state fits, residual analyses for AHH-D(I)MA and DMA', and tabulated pressure-volume data for the ammonia hydrate and H_2O ice phases.

[33] Y. Fei, A. Ricolleau, M. Frank, K. Mibe, G. Shen, and V. Prakapenka, Toward an internally consistent pressure scale, Proc. Natl. Acad. Sci. USA **104**, 9182 (2007).

[34] K. Takemura and A. Dewaele, Isothermal equation of state for gold with a He-pressure medium, Phys. Rev. B **78**, 104119 (2008).

[35] R. Hrubiak, J. S. Smith, and G. Shen, Multimode scanning X-ray diffraction microscopy for diamond anvil cell experiments, Rev. Sci. Instrum. **90**, 025109 (2019).

[36] J. Gonzalez-Platas, M. Alvaro, F. Nestola, and R. Angel, *EosFit7-GUI* : A new graphical user interface for equation of state calculations, analyses and teaching, J. Appl. Crystal. **49**, 1377 (2016).

[37] C. Ma, F. Li, Q. Zhou, F. Huang, J. Wang, M. Zhang, Z. Wang, and Q. Cui, Ammonia molecule rotation of pressure-induced

phase transition in ammonia hemihydrates $2NH_3 \cdot H_2O$, RSC Adv. **2**, 4920 (2012).

[38] L. Andriambariarijaona, F. Datchi, H. Zhang, K. Béneut, B. Baptiste, N. Guignot, and S. Ninet, High pressure–temperature phase diagram of ammonia hemihydrate, Phys. Rev. B **108**, 174102 (2023).

[39] W. Xu, V. N. Robinson, X. Zhang, H.-C. Zhang, M.-E. Donnelly, P. Dalladay-Simpson, A. Hermann, X.-D. Liu, and E. Gregoryanz, Ionic phases of ammonia-rich hydrate at high densities, Phys. Rev. Lett. **126**, 015702 (2021).

[40] C. Liu, A. Mafety, J. A. Queyroux, C. W. Wilson, H. Zhang, K. Béneut, G. Le Marchand, B. Baptiste, P. Dumas, G. Garbarino, F. Finocchi, J. S. Loveday, F. Pietrucci, A. M. Saitta, F. Datchi, and S. Ninet, Topologically frustrated ionisation in a water-ammonia ice mixture, Nat. Commun. **8**, 1065 (2017).

[41] H. Zhang, F. Datchi, L. Andriambariarijaona, M. Rescigno, L. E. Bove, S. Klotz, and S. Ninet, Observation of a plastic crystal in water–ammonia mixtures under high pressure and temperature, J. Phys. Chem. Lett. **14**, 2301 (2023).

[42] H. Zhang, Experimental investigation of the phase diagram of ammonia monohydrate at high pressure and temperature, Ph.D. thesis, HAL Sorbonne Université, 2019, https://theses.hal.science/tel-03459424.

[43] J. S. Loveday and R. J. Nelmes, Ammonia monohydrate VI: A hydrogen-bonded molecular alloy, Phys. Rev. Lett. **83**, 4329 (1999).

[44] S. Klotz, K. Komatsu, H. Kagi, K. Kunc, A. Sano-Furukawa, S. Machida, and T. Hattori, Bulk moduli and equations of state of ice VII and ice VIII, Phys. Rev. B **95**, 174111 (2017).

[45] F. Datchi, S. Ninet, M. Gauthier, A. M. Saitta, B. Canny, and F. Decremps, Solid ammonia at high pressure: A single-crystal x-ray diffraction study to 123 GPa, Phys. Rev. B **73**, 174111 (2006).

[46] S. Berni, D. Scelta, S. Fanetti, and R. Bini, High pressure behavior of ethylene and water: From clathrate hydrate to polymerization in solid ice mixtures, J. Chem. Phys. **158**, 064505 (2023).

[47] X. Wei, X. Li, Z. Zhang, H.-P. Liermann, S. Speziale, M. Pu, C. Zhang, R. Li, H. Yu, L. Li, F. Li, and Q. Zhou, Impact of $CaCl_2$ -induced chemical pressure on the phase transition of H_2O at high pressure, Phys. Rev. B **109**, 134108 (2024).

[48] H. Zhang, F. Datchi, L. M. Andriambariarijaona, G. Zhang, J. A. Queyroux, K. Béneut, M. Mezouar, and S. Ninet, Melting curve and phase diagram of ammonia monohydrate at high pressure and temperature, J. Chem. Phys. **153**, 154503 (2020).

[49] A. S. J. Méndez, F. Trybel, R. J. Husband, G. Steinle-Neumann, H.-P. Liermann, and H. Marquardt, Bulk modulus of H_2O across the ice VII–ice X transition measured by time-resolved x-ray diffraction in dynamic diamond anvil cell experiments, Phys. Rev. B **103**, 064104 (2021).

[50] B. Journaux, I. Daniel, S. Petitgirard, H. Cardon, J.-P. Perrillat, R. Caracas, and M. Mezouar, Salt partitioning between water and high-pressure ices. Implication for the dynamics and habitability of icy moons and water-rich planetary bodies, Earth Planet. Sci. Lett. **463**, 36 (2017).

[51] M. R. Frank, C. E. Runge, H. P. Scott, S. J. Maglio, J. Olson, V. B. Prakapenka, and G. Shen, Experimental study of the NaCl-H_2O system up to 28 GPa: Implications for ice-rich planetary bodies, Phys. Earth Planet. Inter. **155**, 152 (2006).

[52] M. R. Frank, E. Aarestad, H. P. Scott, and V. B. Prakapenka, A comparison of ice VII formed in the H_2O, NaCl-H_2O, and CH_3OH-H_2O systems: Implications for H_2O-rich planets, Phys. Earth Planet. Inter. **215**, 12 (2013).

[53] C. W. Kammeyer and D. R. Whitman, Quantum mechanical calculation of molecular radii. I. hydrides of elements of periodic groups IV through VII, J. Chem. Phys. **56**, 4419 (1972).

[54] S. Klotz, L. E. Bove, T. Strässle, T. C. Hansen, and A. M. Saitta, The preparation and structure of salty ice VII under pressure, Nature Mater **8**, 405 (2009).

[55] https://gitlab.desy.de/rachel.husband/peakfit.